nature communications

Article

https://doi.org/10.1038/s41467-024-55359-8

Substrate transport and drug interaction of human thiamine transporters SLC19A2/A3

Received: 21 May 2024

Accepted: 9 December 2024

Published online: 30 December 2024

Check for updates

Peipei Li[1,2,3,6], Zhini Zhu[1,6], Yong Wang[2,6] ✉, Xuyuan Zhang[2,6], Chuanhui Yang[1,6], Yalan Zhu[4,6], Zixuan Zhou[1], Yulin Chao[1], Yonghui Long[1], Yina Gao[2], Songqing Liu[2], Liguo Zhang[2,3] ✉, Pu Gao[2,3,5] ✉ & Qianhui Qu[1] ✉

Thiamine and pyridoxine are essential B vitamins that serve as enzymatic cofactors in energy metabolism, protein and nucleic acid biosynthesis, and neurotransmitter production. In humans, thiamine transporters SLC19A2 and SLC19A3 primarily regulate cellular uptake of both vitamins. Genetic mutations in these transporters, which cause thiamine and pyridoxine deficiency, have been implicated in severe neurometabolic diseases. Additionally, various prescribed medicines, including metformin and fedratinib, manipulate thiamine transporters, complicating the therapeutic effect. Despite their physiological and pharmacological significance, the molecular underpinnings of substrate and drug recognition remain unknown. Here we present ten cryo-EM structures of human thiamine transporters SLC19A3 and SLC19A2 in outward- and inward-facing conformations, complexed with thiamine, pyridoxine, metformin, fedratinib, and amprolium. These structural insights, combined with functional characterizations, illuminate the translocation mechanism of diverse chemical entities, and enhance our understanding of drug-nutrient interactions mediated by thiamine transporters.

B vitamins, including thiamine (vitamin B1) and pyridoxine (vitamin B6), are a group of water-soluble, chemically varied compounds that perform important roles in bodily functions including normal growth and development[1]. Dietary intake of these vitamins is indispensable, as they cannot be synthesized de novo in humans and other mammals[2]. Thiamine is absorbed in the small intestine and rapidly converted to its active form, thiamine pyrophosphate (TPP), which constitutes the primary thiamine store and acts as a key coenzyme in the release of energy from carbohydrates, RNA and DNA synthesis, and nerve activity[3]. Likewise, the metabolically active form of pyridoxine after cellular absorption, pyridoxal 5′-phosphate (PLP), acts as an essential cofactor in numerous enzymatic reactions, primarily in amino acid metabolism including the biosynthesis of neurotransmitters[4].

Two solute carriers SLC19A2 and SLC19A3, identified as high-affinity thiamine transporters, have been demonstrated largely responsible for moving cationic thiamine and pyridoxine across the plasma membrane[5–7]. SLC19A2 is widely distributed in human tissues but is highly enriched in the skeletal muscle, while SLC19A3 is most abundant in placenta followed by liver, kidney, and heart[8]. Genetic mutations of SLC19A2 cause a thiamine-responsive megaloblastic anemia syndrome (TRMA), an autosomal recessive disorder featuring diabetes mellitus, megaloblastic anemia, and sensorineural deafness[9],

[1]ENT Institute and Otorhinolaryngology Department of Eye & ENT Hospital, Institutes of Biomedical Sciences, Shanghai Key Laboratory of Medical Epigenetics, International Co-laboratory of Medical Epigenetics and Metabolism (Ministry of Science and Technology), Department of Systems Biology for Medicine, Fudan University, Shanghai, China. [2]Key Laboratory of Biomacromolecules (CAS), National Laboratory of Biomacromolecules, CAS Center for Excellence in Biomacromolecules, Institute of Biophysics, Chinese Academy of Sciences, Beijing, China. [3]University of Chinese Academy of Sciences, Beijing, China. [4]School of Life Sciences, Beijing Institute of Technology, Beijing, China. [5]Science and Technology Innovation Center, Shandong First Medical University & Shandong Academy of Medical Sciences, Jinan, China. [6]These authors contributed equally: Peipei Li, Zhini Zhu, Yong Wang, Xuyuan Zhang, Chuanhui Yang, Yalan Zhu. ✉e-mail: wangyong@ibp.ac.cn; liguozhang@ibp.ac.cn; gaopu@ibp.ac.cn; qqh@fudan.edu.cn

which has been phenocopied by targeted disruption of the equivalent SLC19A2 gene in mice[10]. Mutations in SLC19A3 are associated with Wernicke's-like encephalopathy[11] and biotin- and thiamine-responsive basal ganglia disease (BTBGD)[12–14], which may reflect the critical role of SLC19A3 in maintaining thiamine levels in the blood and brain[15,16]. Notably, TRMA patients often do not exhibit other neurological or cardiac symptoms of thiamine deficiency that are seen in SLC19A3-related diseases[17]. Despite the potentially fatal consequences, some symptoms can be alleviated by receiving high dosages of thiamine supplements[2], potentially via alternate absorption routes, such as the low-affinity, high-capacity nonspecific organic cation transporter 1 (OCT1)[18]. Aside from thiamine and pyridoxine import, thiamine transporters are also influenced by several cationic medicines, including the antidiabetic metformin, the antidepressant amitriptyline, the antineoplastic fedratinib, and the antibiotics amprolium[19–22]. Caution should be exercised when using these drugs, since transporter-mediated drug-nutrient interactions would predispose the patients to thiamine and pyridoxine deficiencies[20,23,24].

SLC19A2 and SLC19A3, together with the homologous folate transporter SLC19A1, constitute the vitamin-transporting SLC19 subfamily, which belongs to the Major Facilitator Superfamily (MFS)[25,26]. Despite extensive functional characterization of the transport activity, drug-nutrient interactions, and genetic mutation mapping, the precise molecular basis of substrate transport and drug/inhibitor recognition by SLC19A2 and SLC19A3 has yet to be fully explored. Recent structural advancements in SLC19A1 have provided great insight into folate transportation[27–29]. However, unlike SLC19A1 which distributes the anionic folate, SLC19A2 and SLC19A3 shuttle cationic thiamine and pyridoxine under physiological pH conditions. Thus, an understanding of SLC19A1 transport mechanism may not be directly applicable to SLC19A2 and SLC19A3.

In this study, we determined ten cryo-EM structures of SLC19A3 and SLC19A2 with a variety of substrates and drugs, in the outward- and inward-facing conformations. Complemented by biochemical and cellular analysis, these conformational snapshots revealed shared features as well as unique elements of both transporters for vitamin transport and drug recognition.

Results

Structural determination of human SLC19A2 and SLC19A3

Thiamine transporters (~55 kDa) lack discernable extramembrane domains apart from the 12 transmembrane helices (TMs). To facilitate the cryo-EM analysis, we immunized mice with a shorter version of the human SLC19A3 construct (residues 6-472) that lacks the disordered but highly immunogenic N- and C-termini ($SLC19A3_{cryo}$, Supplementary Fig. 1a). We isolated a high-affinity fragment antigen-binding region (Fab) against SLC19A3, and successfully determined the cryo-EM structures of SLC19A3-Fab in the apo state and in complex with thiamine, pyridoxine, fedratinib, amprolium, and metformin (Fig. 1 and Supplementary Figs. 1–4). The truncated construct ($SLC19A3_{cryo}$) showed the radiolabeled thiamine (^{3}H-thiamine) uptake activity similar to wild-type in stably transfected HEK293T cells (Supplementary Fig. 1d), therefore it was still referred to as SLC19A3 hereafter. Notably, all of these SLC19A3 structures were captured in the outward-facing state by the intracellular side Fab binder, implying a conformation-specific antibody generated by the antigen vaccination strategy.

To aid in the structural identification of SLC19A3, we also employed a different strategy by adding a helical MPER peptide prior to the amino-end of TM1 helix ($SLC19A3_{MPER}$) and assembling a stable complex with its high-affinity antibody (Fab_10E8v4, Supplementary Fig. 1b)[30]. $SLC19A3_{MPER}$ retains robust ^{3}H-thiamine uptake in HEK293T cells, with activity levels approximately half those of wild-type SLC19A3, possibly due to perturbed surface localization (Supplementary Fig. 1d); therefore, this MPER-fusion construct was also denoted as SLC19A3 for simplicity. Interestingly, such an approach enabled the capture of SLC19A3 in a distinct inward-facing conformation, either in the presence of thiamine or the antineoplastic drug fedratinib (Fig. 1 and Supplementary Fig. 5).

We also used the same MPER-fusion approach for human SLC19A2. In accordance, the N-terminal 30 residues of SLC19A2 were removed to design the continuous helix formation of MPER segment with TM1 ($SLC19A2_{MPER}$, Supplementary Fig. 1c). The $SLC19A2_{MPER}$ protein accumulated moderately less ^{3}H-thiamine compared to wild-type in HEK293 cells (Supplementary Fig. 1f), likely due to the decreased surface expression, as shown by Said and colleagues that the N-terminal sequence (residues 19-29) is important for cell surface localization of SLC19A2[31]. For simplicity, the fusion construct is still referred to as SLC19A2. By using the same MPER-Fab binder, we obtained the inward-facing conformation of SLC19A2 in complex with either thiamine or pyridoxine (Fig. 1 and Supplementary Figs. 3–6). Notably, the relative orientation of this MPER/Fab differs in the two closely related transporters (Supplementary Fig. 7a), as the MPER segment failed to form a seamless helix with SLC19A2 TM1, probably because of the variation in junction residues (Phe30/Leu31 in hSLC19A2 vs Ile13/Tyr14 in hSLC19A3, Supplementary Fig. 8).

Thiamine recognition and transport in SLC19A3

As expected, apo SLC19A3 adopts the canonical MFS fold, with the translocation passage formed between two pseudo-symmetrically related domains: N-domain TMs 1-6, and C-domain TMs 7-12. Two helical bundles are connected by a long intracellular linker (Lys194 to Lys276) between TM6 and TM7 (Fig. 2a, b). A well-resolved density for an amphipathic helical stretch (Phe262-Cys272) in the outward-facing map is embedded parallelly in the membrane. Deletion or replacement of this helical stretch did not significantly affect the ^{3}H-thiamine transport capacity of SLC19A3 (Supplementary Fig. 9). Compared to the 3.15-Å resolution apo SLC19A3 map, both the 3.0-Å outward-facing and the 3.36-Å inward-facing maps with thiamine supplemented exhibit an additional density that fits well for a thiamine molecule in the translocation funnel (Fig. 2c–f). It is worthy to note that the local resolution around the ligand binding pocket is notably high, enabling confident modeling of the ligands and surrounding residues (Supplementary Figs. 2–6), which is further supported by relative stability during molecular dynamics simulations (Supplementary Fig. 10). The electropositive thiamine sits snugly in the overall electronegative cavity, which is positioned close to the extracellular side of SLC19A3 TMD (Fig. 2c and e). Such a superficial location of substrate binding pocket is reminiscent of the homologous SLC19A1 bound by folate[27–29].

Comparison of the thiamine-bound outward- and inward-facing SLC19A3 structures reveals that the transporter adopts a similar rocker-switch movement as seen in other MFS members. Notably, SLC19A3 pivots at one-third of the funnel axis, close to the extracellular side, whereas other MFS transporters typically rock around the central site[25,26]. A closer look at the thiamine binding pocket reveals both similarities and differences between the outward- and inward-facing states. In the outward-facing conformation, thiamine is mainly embraced by residues from the N-domain (Fig. 2d). Specifically, the aminopyrimidine ring of thiamine wedges deeply into the N-domain helical bundle along the horizontal membrane plane, and stacks against Tyr113 on TM4 and, to a lesser extent, Trp59 on TM2 via π-π interactions. The primary amine and the adjacent ring-nitrogen fully engage with Glu110 on TM4 through hydrogen-bonding. The methyl group on the aminopyrimidine moiety points to a hydrophobic cage lined by Val109 on TM4, and Thr93 and Leu97 on TM3. Linked to the aminopyrimidine by a methylene bridge, the thiazolium ring on the other side of thiamine is bent nearly perpendicular to the aminopyrimidine ring, and faces the ample translocation funnel that establishes π stacking against Phe56 on TM2. Glu32 on the substantially unwound segment of TM1 is in close vicinity of the second ring-nitrogen of aminopyrimidine (3.4 Å) and the positively charged thiazolium

https://doi.org/10.1038/s41467-024-55359-8

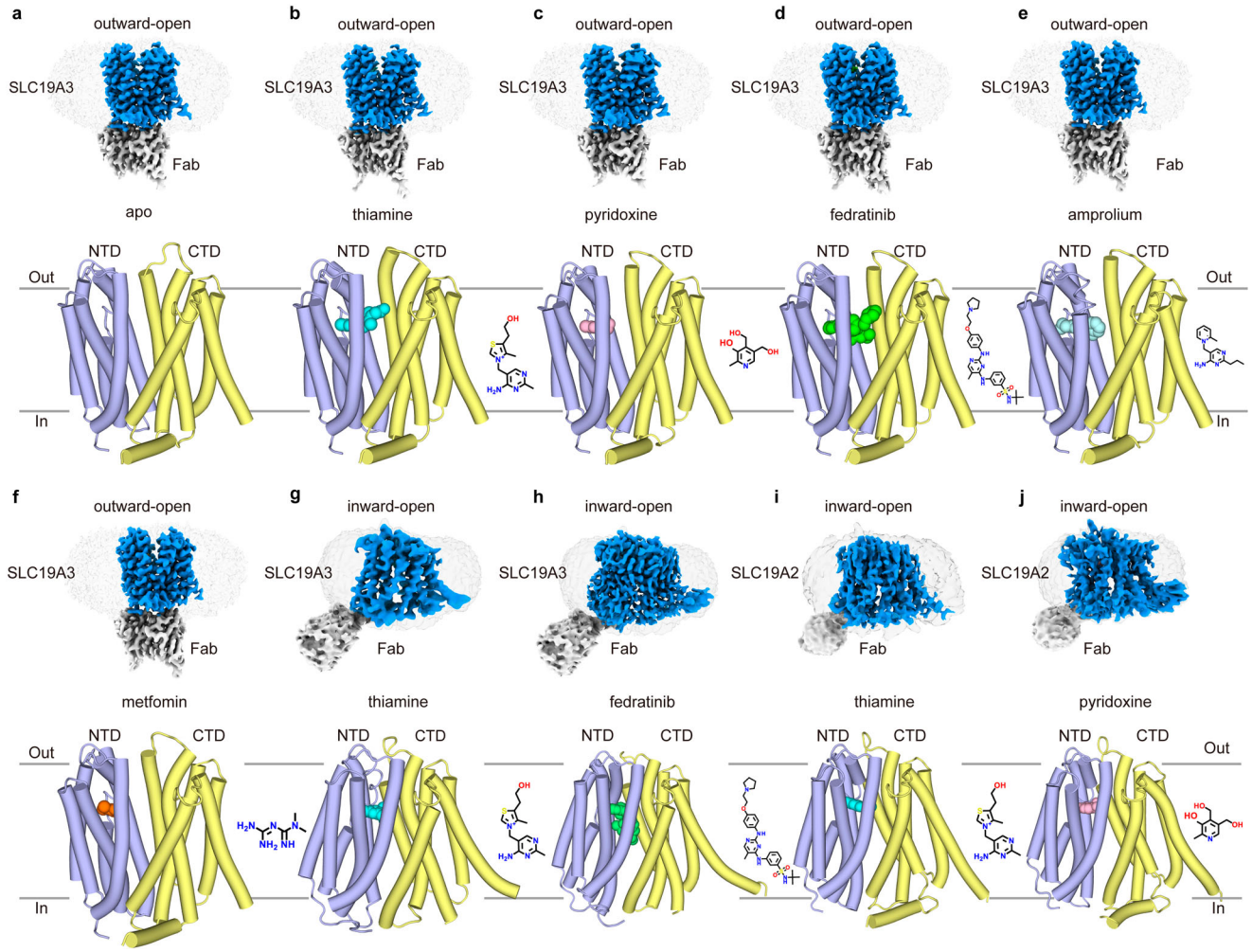

Fig. 1 | Structures of human SLC19A3 and SLC19A2 in complex with different ligands. a Cryo-EM density map of apo SLC19A3 (blue)–Fab (grey) in an outward-open conformation (top), with N- and C-terminal domains (NTD and CTD) colored blue and yellow in structural model (bottom), respectively. Cryo-EM density (top) and structural model (bottom) of SLC19A3 bound to thiamine (cyan) (**b**), pyridoxine (pink) (**c**), fedratinib (green) (**d**), amprolium (pale cyan) (**e**) and metformin (orange) (**f**) in an outward-open conformation. The 2D chemical structure of ligands are shown in accordance. Cryo-EM density (top) and structure (bottom) of SLC19A3 bound to thiamine (**g**) and fedratinib (**h**) in an inward-open conformation. Cryo-EM density (top) and structure (bottom) of SLC19A2 bound to thiamine (**i**) and pyridoxine (**j**) in an inward-open conformation.

nitrogen (5.5 Å), which may provide additional electrostatic attraction and selectivity for cationic thiamine. The hydroxyethyl tail of thiamine is approaching the backbone carbonyl oxygen of Asn297 on TM7, the only contact with the C-domain bundle in the outward-facing conformation.

Along with the conformational transition of SLC19A3 from outward-facing to inward-facing state, thiamine exhibits a substantial rearrangement. In the inward-facing SLC19A3 structure, the thiamine molecule adopts a more extended conformation, compared to the bent posture in the outward-facing state (Fig. 2e). While the aminopyrimidine moiety of thiamine remains accommodated by the similar set of residues on N-domain, the thiazolium ring swings away from Phe56 toward the interior of translocation funnel. This substantial movement establishes the primary amine on aminopyrimidine ring bonding with Asn297, reorients the thiazolium ring sandwiched between TM1 and TM7, moves the thiazolium nitrogen closer to Glu32 (4.8 Å), and approaches the hydroxyethyl tail to Glu320 on TM8. Moreover, additional interactions between thiamine and Tyr151, Leu296, and Gln300 are also established (Fig. 2f). Thus, the thiamine is fully coordinated by both N-domain and C-domain when SLC19A3 transits from outward- to inward-facing state. The interaction network is further validated by our mutagenesis analysis on the cellular uptake of ^{3}H-thiamine (Fig. 2g and Supplementary Fig. 1e). Notably, the positive effects of residues Arg29 and Lys380 on thiamine uptake were unexpected, as they do not directly contact thiamine (Fig. 2g). A closer examination of the thiamine-SLC19A3 binding environment reveals that both residues may play a role in the transport activity by maintaining a proper interaction network through hydrogen bonding with Glu32/Tyr113 (Arg29) and Glu320 (Lys380), which are critical for substrate recognition.

Unique features in thiamine-SLC19A2 interaction

Human SLC19A2 is the first identified high-affinity thiamine transporter[5], which shares ~48% sequence identity with its close homolog SLC19A3 (Supplementary Fig. 8). Both transporters can transport thiamine efficiently, while SLC19A2 has a slightly larger *K*m and higher import *V*max values than SLC19A3, and their transport profiles can be altered differently by pH conditions, suggesting different mechanisms underlying SLC19A2 and SLC19A3-mediated thiamine absorption[5–7]. To address this issue, we first measured the thiamine binding affinity with purified SLC19A2 or SLC19A3 in different pH buffers via a microscale thermophoresis (MST) assay (Fig. 3). At pH 7.5, thiamine exhibits a comparable affinity with both SLC19A2 (*K*d ~ 78.4 μM) and SLC19A3 (*K*d ~ 153.7 μM, Fig. 3a), consistent with the

https://doi.org/10.1038/s41467-024-55359-8

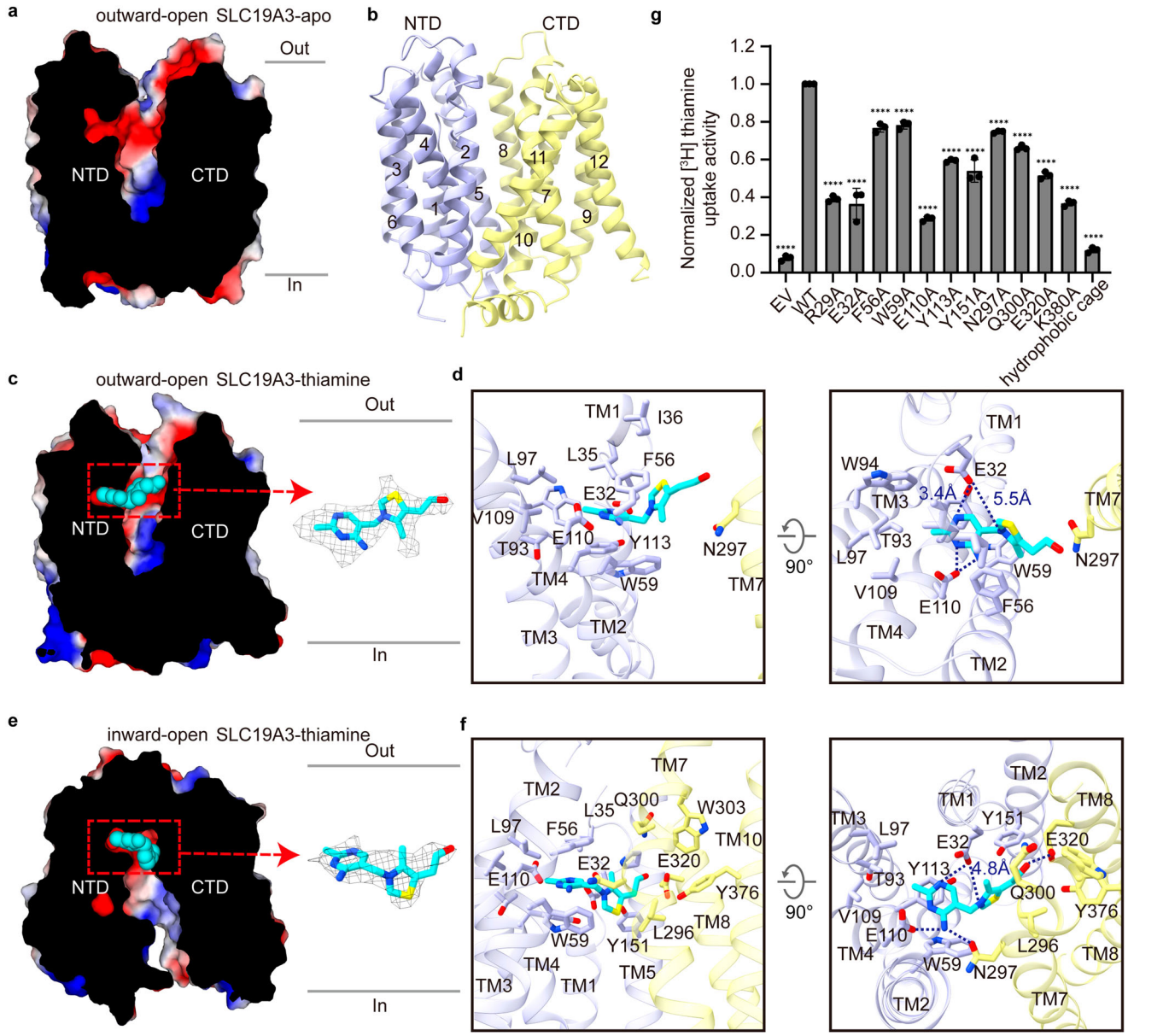

Fig. 2 | Thiamine recognition and transport in SLC19A3. a Cut-open view of apo SLC19A3 outward-open structure, rendered by electrostatic potential (red to blue, −50 kT/e to +50 kT/e). **b** Cartoon representation of the SLC19A3 outward-open structure, with N- and C-terminal domains (NTD and CTD) colored blue and yellow, respectively. **c** Thiamine binding pocket of SLC19A3 in the outward-open conformation. **d** Detailed interactions between thiamine and SLC19A3 in the outward-open conformation. **e** Thiamine binding site of SLC19A3 in the inward-open conformation. **f** Detailed interactions between thiamine and SLC19A3 in the inward-open conformation. **g** [^{3}H] thiamine uptake activity of SLC19A3 mutants in stably transfected HEK 293 T cells. Data were normalized to WT and are presented as mean ± SEM of $n = 3$ biologically independent experiments. Statistical analysis was performed using two-tailed unpaired Student's-tests. ****$P \le 0.0001$; EV, empty vector; WT, SLC19A3 wild type; hydrophobic cage, L35A/I36A/T93A/W94A/L97A/V109A.

reported *K*m difference[7]. Surprisingly, thiamine binds more strongly to SLC19A2 (*K*d ~ 1.2 μM), and even tighter to SLC19A3 (*K*d~0.25 μM) at pH 6.0 (Fig. 3b).

To gain a deeper understanding of the different behavior, we prepared thiamine-bound SLC19A2 sample under the same condition as thiamine-bound SLC19A3$_{MPER}$, and determined a 3.28-Å inward-facing structure at pH 6.0 (Supplementary Fig. 5). As expected, the overall structure of SLC19A2 is similar to that of SLC19A3, with the main chain Cα root mean standard deviation (RMSD) of 0.8 Å (Supplementary Fig. 7b). Consistently, thiamine occupies the cavity of similar interaction elements on SLC19A2 as described above for SLC19A3 (Fig. 3e and f), which is consistent with alterations in cellular uptake capacity of ^{3}H-thiamine upon alanine substitution of pocket residues (Fig. 3k). However, closer inspection into the substrate pocket did reveal some unique features. First, residues Tyr74, Leu127, Phe169 and Val313 on SLC19A2 are replaced by Phe56, Val109, Tyr151, and Leu296 at equivalent positions on SLC19A3 (Supplementary Fig. 8). In the inward-facing SLC19A3, the thiazolium ring of thiamine is approached by Tyr151 hydroxyl group at its sulfur on one side, and by the hydrophobic Leu296 on the other side (Fig. 2f). Instead, SLC19A2 Phe169 lacks the hydroxyl group, while Val313 has a shorter side chain. Second, Asn297 establishes a hydrogen bond with the primary amine group of thiamine in SLC19A3, while the counterpart Asn314 of SLC19A2 orients away from thiamine (Fig. 3f). Therefore, these minor but significant variations may contribute to a slightly lower affinity of thiamine for SLC19A2 than for SLC19A3, resulting in divergent kinetics for the two transporters.

https://doi.org/10.1038/s41467-024-55359-8

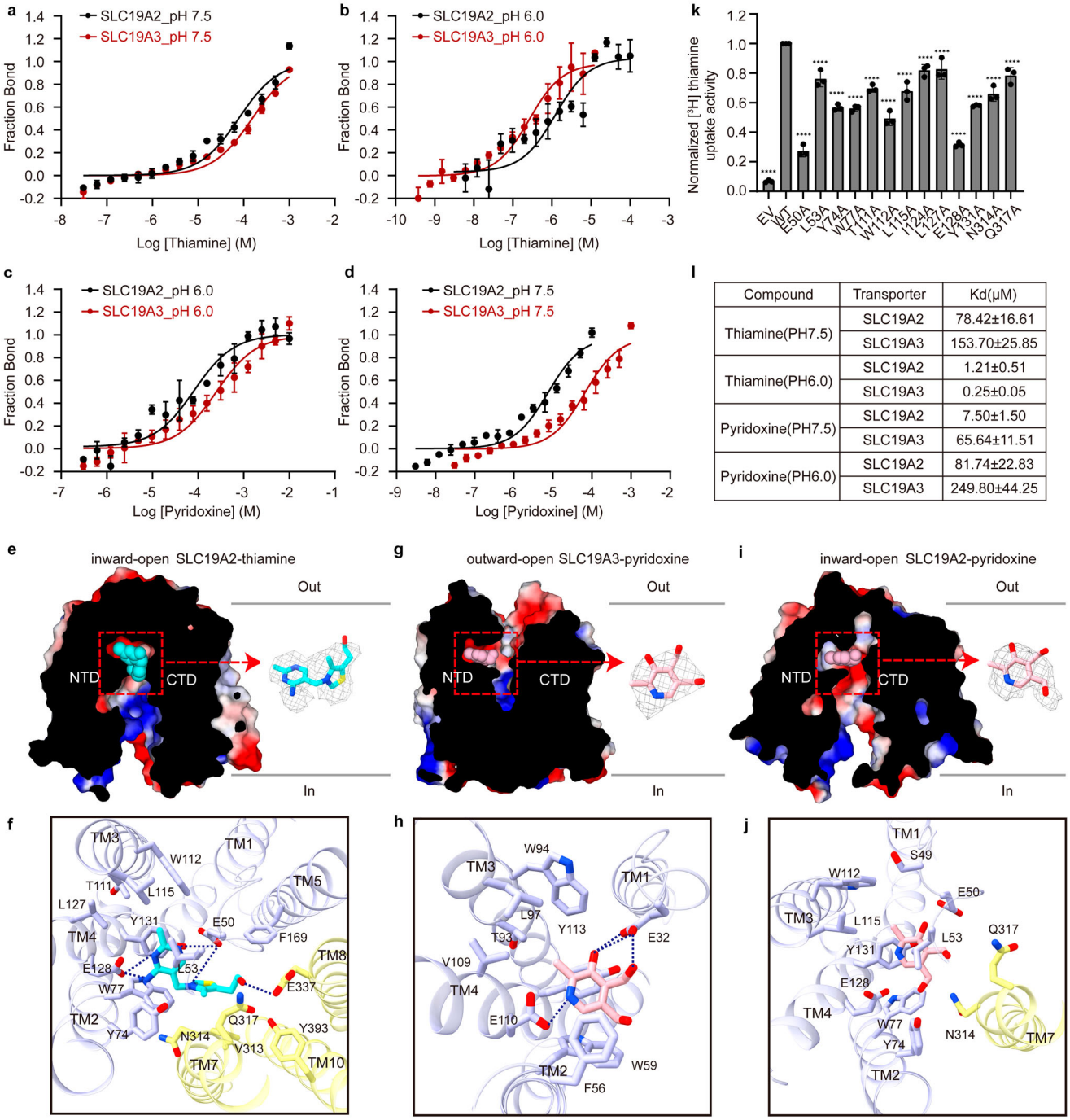

Compound	Transporter	Kd(μM)
Thiamine(PH7.5)	SLC19A2	78.42±16.61
	SLC19A3	153.70±25.85
Thiamine(PH6.0)	SLC19A2	1.21±0.51
	SLC19A3	0.25±0.05
Pyridoxine(PH7.5)	SLC19A2	7.50±1.50
	SLC19A3	65.64±11.51
Pyridoxine(PH6.0)	SLC19A2	81.74±22.83
	SLC19A3	249.80±44.25

Fig. 3 | Comparison of thiamine and pyridoxine binding in SLC19A2 and SLC19A3. Binding affinity for SLC19A2 and SLC19A3 with thiamine at pH 7.5 (**a**) and pH 6.0 (**b**) and with pyridoxine at pH 6.0 (**c**) and pH 7.5 (**d**) measured using microscale thermophoresis (MST) assay (mean ± SEM, $n = 3$ independent experiments). Localization of thiamine in the inward-open SLC19A2 (**e**), pyridoxine in the outward-open SLC19A3 (**g**) and pyridoxine in the inward-open SLC19A2 structure (**i**). Detailed interactions between thiamine and SLC19A2 in the inward-open conformation (**f**), pyridoxine and SLC19A3 in the outward-open conformation (**h**) and pyridoxine and SLC19A3 in the outward-open conformation (**j**). Residues involved in thiamine and pyridoxine binding are depicted as sticks. Hydrogen bonds are indicated by blue dashed lines. **k** [^{3}H] thiamine uptake activity of SLC19A2 mutants in stably transfected HEK 293 T cells. Data were normalized to WT and are presented as mean ± SEM of $n = 3$ biologically independent experiments. Statistical analysis was performed using two-tailed unpaired Student's-tests. ****$P \le 0.0001$; EV, empty vector; WT, SLC19A2 wild type. **l** Summary of binding affinity via MST (mean ± SEM, $n = 3$ independent experiments).

Pyridoxine binding sites on SLC19A2 and SLC19A3

Thiamine transporters SLC19A2/A3 have been recently identified as the long-seeking carrier for pyridoxine (vitamin B_6) absorption, a protonophore-sensitive process that favors acidic conditions over neutral to basic conditions[7]. Our MST measurements revealed that pyridoxine binds relatively weaker to SLC19A2 (*K*d-249.8 μM) than to SLC19A3 (*K*d-81.7 μM) at pH 6.0 (Fig. 3c), consistent with previous cellular uptake *K*m values[7]. Interestingly, both transporters showed substantially increased affinity for pyridoxine at pH 7.5 (Fig. 3d).

To understand the molecular mechanism for pyridoxine recognition and transportation, we further determined the structures of pyridoxine in complex with SLC19A3 and SLC19A2 (Supplementary Figs. 4–6). The outward-facing pyridoxine-bound SLC19A3 structure is nearly identical to thiamine-bound SLC19A3 (Cα RMSD 0.43 Å,

Supplementary Fig. 7c), with pyridoxine inserted at the similar cavity to thiamine and embraced by almost the same set of residues exclusively on the N-domain (Fig. 3g and h), which remains stable during MD simulations (Supplementary Fig. 10). Specifically, the pyridine ring is clamped by Phe56 and Tyr113 through π-π stacking, contacted by Glu32 and Glu110 via hydrogen bonding, and buttressed by Trp59, Thr93, Trp94, Leu97 and Val109 upon hydrophobic interaction (Fig. 3h). Likewise, the inward-facing pyridoxine-bound SLC19A2 structure is also similar to thiamine-bound SLC19A2 (Cα RMSD 1.04 Å, Supplementary Fig. 7d), with pyridoxine occupying the same cluster of hydrophilic or hydrophobic residues in thiamine binding site (Fig. 3i and j). These observations thus corroborate the notion that pyridoxine is a competitive substrate for thiamine transporters[7]. Notably, pyridoxine, a bipolar molecule with pKa values of 5.6 and 9.4, can exist in different protonation states under acidic, neutral, and basic conditions. As pH decreases from near neutral (e.g., pH 7.5) to acidic (e.g., pH 6.0), pyridoxine becomes increasingly cationized. Interestingly, residues like Glu128 in SLC19A2 and Glu110 in SLC19A3, which interact with pyridoxine's amine group through hydrogen bonding, may also become protonated at pH 6.0. This protonation could disrupt the hydrogen bond, thereby weakening pyridoxine's interaction with the transporters at lower pH conditions.

Inhibition of SLC19A3 by antineoplastic fedratinib

Fedratinib (Inrebic®) is a newly FDA-approved selective inhibitor of Janus kinase 2 (JAK-2) to treat myeloproliferative diseases including myelofibrosis[32], with a boxed warning regarding the risk of potentially fatal encephalopathy. The clinical development of fedratinib was halted in 2013, when several cases consistent with Wernicke's encephalopathy were reported in some participants[20]. We confirmed the inhibitory effect of fedratinib on both SLC19A2- and SLC19A3-mediated thiamine absorption in HEK293T cells (Fig. 4a), and assessed the direct binding of fedratinib to purified SLC19A3 (*K*d ~ 0.42 μM), and to a lesser extent to SLC19A2 (*K*d~13.73 μM), by the MST assay (-Fig. 4b). The difference in in vitro binding affinity likely underpins the mechanism that fedratinib inhibits thiamine uptake by SLC19A3 slightly stronger than by SLC19A2 (IC50: 1.09 μM for SLC19A3 vs 10.7 μM for SLC19A2, respectively)[22]. We then determined the structures of SLC19A3 with fedratinib in the outward- and inward-facing conformations at 3.1-Å and 3.0-Å resolution, respectively (Supplementary Figs. 4–6).

Both fedratinib-bound structures share an overall similar architecture with the corresponding thiamine-bound outward-facing (Cα RMSD 0.37 Å) and inward-facing SLC19A3 (Cα RMSD 0.73 Å), respectively (Supplementary Fig. 7e and f). In the outward-facing structure, fedratinib adopts a bent conformation with its two semi-equal length branches kinking around the 2,4-diaminopyrimidine moiety (Fig. 4c). Interestingly, this 2,4-diaminopyrimidine group occupies the same position as the aminopyridine ring of thiamine bound in outward-facing SLC19A3, which allows the establishment of π-π stacking against Tyr113, and hydrogen bonding with two acidic residues Glu32 and Glu110 via its two amine nitrogens. In addition, the benzene ring on the pyrrolidine branch also π-stacks with Phe56 on TM5, a mimic of the thiamine thiazolium ring, and the terminal pyrrolidine ring approaches Asn297, Tyr298 and Ile301 on TM7. On the opposite sulfonamide branch, the sulfonyl group H-bonds with Tyr113 and is proximal to Arg29 on TM1, and the distal hydrophobic tert-butyl group is close to Tyr151 and Leu296 (Fig. 4d).

In the inward-facing state, however, fedratinib adopts an even more compact conformation (Fig. 4e). Although the diaminopyrimidine group and the sulfonamide branch remain in nearly the same position as that in the outward-facing state, the pyrrolidine branch swings away from Phe56 and bends toward the intracellular exit, with the benzene ring T-stacking against Trp59 indole group and the pyrrolidine ring facing its sulfonamide group (Fig. 4f). This conformational rearrangement of fedratinib is similar to that of the thiamine transitions from outward- to inward-facing state. These features further support the concept that fedratinib inhibits thiamine transporters by structurally mimicking thiamine[20].

Metformin and amprolium interactions with SLC19A3

Thiamine-like drugs and other structurally unrelated cationic compounds have been demonstrated interaction with thiamine transporters[21,22]. Our cellular ^{3}H-thiamine uptake assays confirmed the inhibitory effects of thiamine analogues (amprolium, oxythiamine, trimethoprium, pyrimethamine), tyrosine kinase inhibitors (fedratinib, momelotinib, imatinib), antidepressant sertraline, as well as metformin. We further expanded the inhibitor list to include CDKs inhibitor abemaciclib and reverse transcriptase inhibitor etravirine (Supplementary Fig. 11a). Most, if not all, of the drugs have an aminopyrimidine core, a typical characteristic suitable for recognition by thiamine transporters[21,22]. To further elucidate the molecular basis of these compounds in addition to fedratinib, we determined SLC19A3 structures in complex with coccidiostat amprolium and antidiabetic metformin, both in outward-facing conformation at 3.1-Å resolution (Supplementary Figs. 4–6).

In contrast to the bent conformation of thiamine, amprolium adopts an extended pose in the similar binding pocket on SLC19A3 N-domain (Fig. 5a), supported by MD simulation analysis (Supplementary Fig. 10). The aminopyrimidine ring of amprolium overlaps with that of thiamine and is engaged by the same cluster of residues, as anticipated. The propyl chain adorned on pyrimidine ring extends to the hydrophobic cage composed of Thr93, Trp94, Leu97 and Val109. The pyridine ring, a substitute for thiamine's thiazolium ring, stacks nearly face-to-face with Trp59 and edge-to-face against Phe56 (Fig. 5b, c). The semi-conserved interaction network thus maintains a tight contact for amprolium with SLC19A3 and SLC19A2 (*K*d-0.45 μM and ~3.05, respectively) at pH 6.0, with comparable binding affinities to thiamine (Supplementary Fig. 11b).

The metformin-SLC19A3 structure demonstrates a similar coordination network for the biguanide to that of thiamine, albeit without an aminopyrimidine ring (Fig. 5d). Specifically, metformin is clamped by Phe56, Trp59 and Tyr113 via cation-π interactions and balanced by flanking hydrogen bonds with Glu32 and Glu110. The dimethyl substituent inserts into the same hydrophobic cage as described above (Fig. 5e, f). This interaction pattern differs from that of organic cation transporter 1 (OCT1), a well-known carrier for metformin[33], which has a similar millimolar affinity to SLC19A3 (Supplementary Fig. 12). Despite cation-π stacking against neighboring aromatic residues, metformin did not interact with the acidic residues Glu386 or Asp474 in the inward-facing OCT1 structure[34]. Notably, in the same study, the thiamine was also distant from either Glu386 or Asp474 on OCT1 (Supplementary Fig. 12). Nevertheless, our data support the notion that metformin is a substrate and inhibitor of SLC19A3[19].

Discussion

Membrane transporters play a crucial role in the absorption and distribution of nutrients and drugs across biogenic membrane barriers. Significant progress has been achieved in characterizing the functional aspects of cellular thiamine and pyridoxine uptake through high-affinity transporters SLC19A3/THTR-2 and SLC19A2/THTR-1. These transporters, responsible for thiamine and pyridoxine uptake, are potential targets for drug-drug and drug-nutrient interactions. By determining the cryo-EM structures of SLC19A3 and SLC19A2 at different transport states, coupled with the structure-based mutagenesis analysis, here we highlight critical determinants governing the recognition and transport of substrate B vitamins (thiamine and pyridoxine) and therapeutic drugs (metformin, fedratinib, and amprolium) by thiamine transporters.

https://doi.org/10.1038/s41467-024-55359-8

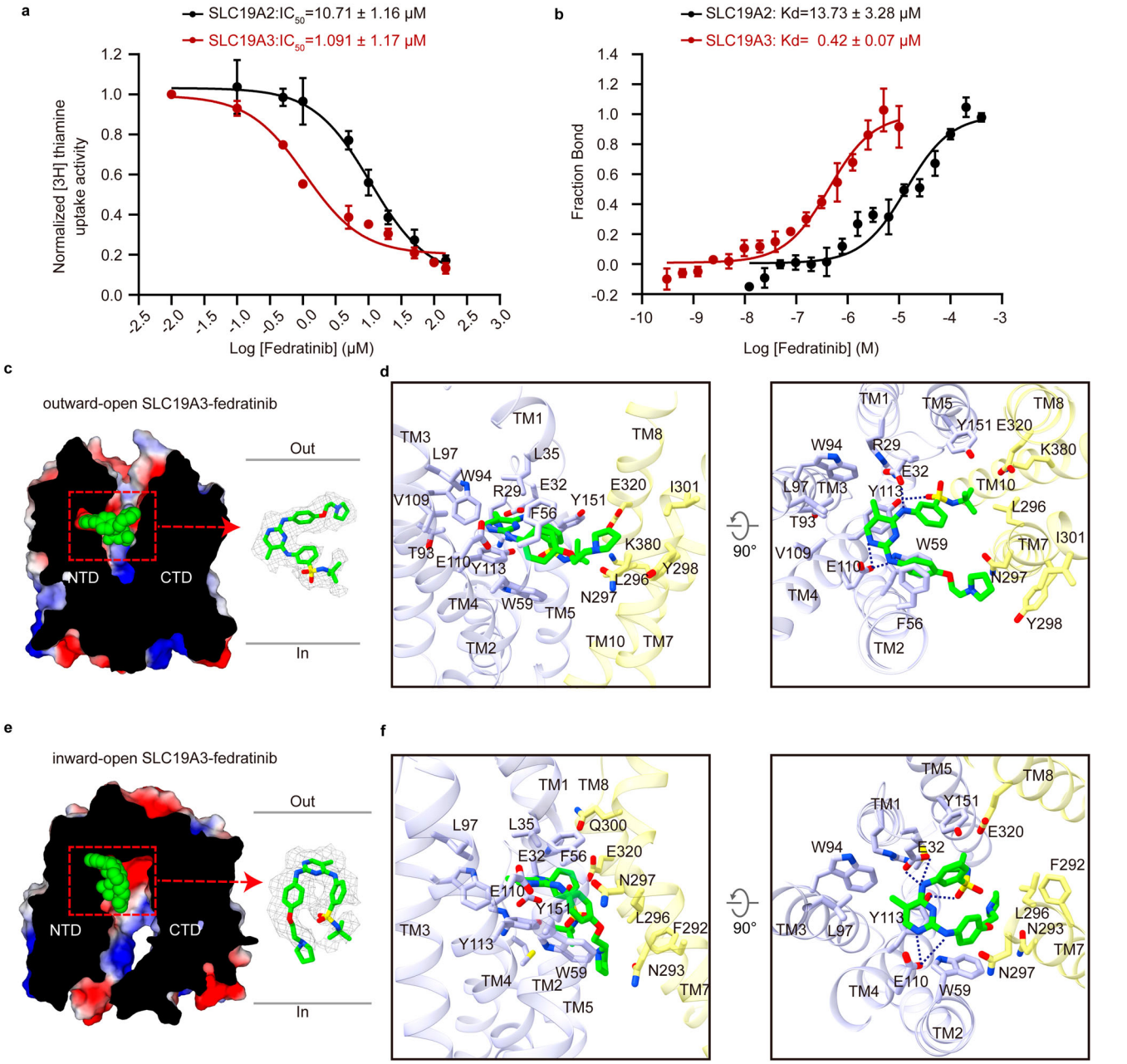

Fig. 4 | Inhibition of thiamine transporters by fedratinib. a Concentration-dependent inhibitory effect of SLC19A2- and SLC19A3-mediated [^{3}H] thiamine uptake by fedratinib. Data are represented in mean ± SEM; $n = 3$ biological replicates. Curves were fitted using nonlinear regression. **b** In vitro binding affinity measure of SLC19A2 and SLC19A3 with fedratinib via MST assay. Localization of fedratinib in the outward-open (**c**) and the inward-open SLC19A3 conformation (**e**), with detailed analysis of ligand binding network shown in (**d**, **f**) accordingly.

It has been proposed that the proton gradient across membrane acts as a driving force for thiamine transporters-mediated ligand movement[7,19,35]. The pH conditions impact SLC19A2- and SLC19A3-mediated thiamine and pyridoxine absorption differently. Our structural and biochemical analyses shed light on this phenomenon. Several acidic residues, including Glu32, Glu110, and Glu320, participate in thiamine and pyridoxine recognition. Notably, genetic mutations of Glu320 have been associated with Wernicke's encephalopathy (E320Q)[11] and BTBGD (E320K)[36], underscoring the significance of this residue. We speculate that interactions between protons and these key residues play pivotal roles in substrate translocation. Notably, residues such as Glu50, Glu128, Glu138, Asp285, and Glu337 in SLC19A2, and Glu54, Asp75, Glu110, and Glu120 in SLC19A3, exhibit differential behaviors within the pH range of 6 ~ 7.5. This variation may contribute to the differences in binding energies between SLC19A2/A3 with thiamine or pyridoxine under varying pH conditions (Supplementary Fig. 10), which roughly aligns with the measured binding affinity values that thiamine exhibits tighter binding with both transporters at pH 6.0, while pyridoxine binds more strongly at pH 7.5 (Fig. 3). This increased ligand binding affinity under certain pH conditions may prolong the duration of ligand-transporter association, thereby influencing the transport cycling rate. This would explain previous observations that thiamine uptake activity peaks around pH 7.4, while pyridoxine transport peaks around pH 5.5[7].

Fedratinib, a recently licensed antineoplastic treatment, selectively targets intracellular JAK2 kinase[20]. Despite extensive pharmacological profiling, its specific absorption mechanism remains unknown. The resemblance between fedratinib and thiamine, both possessing

https://doi.org/10.1038/s41467-024-55359-8

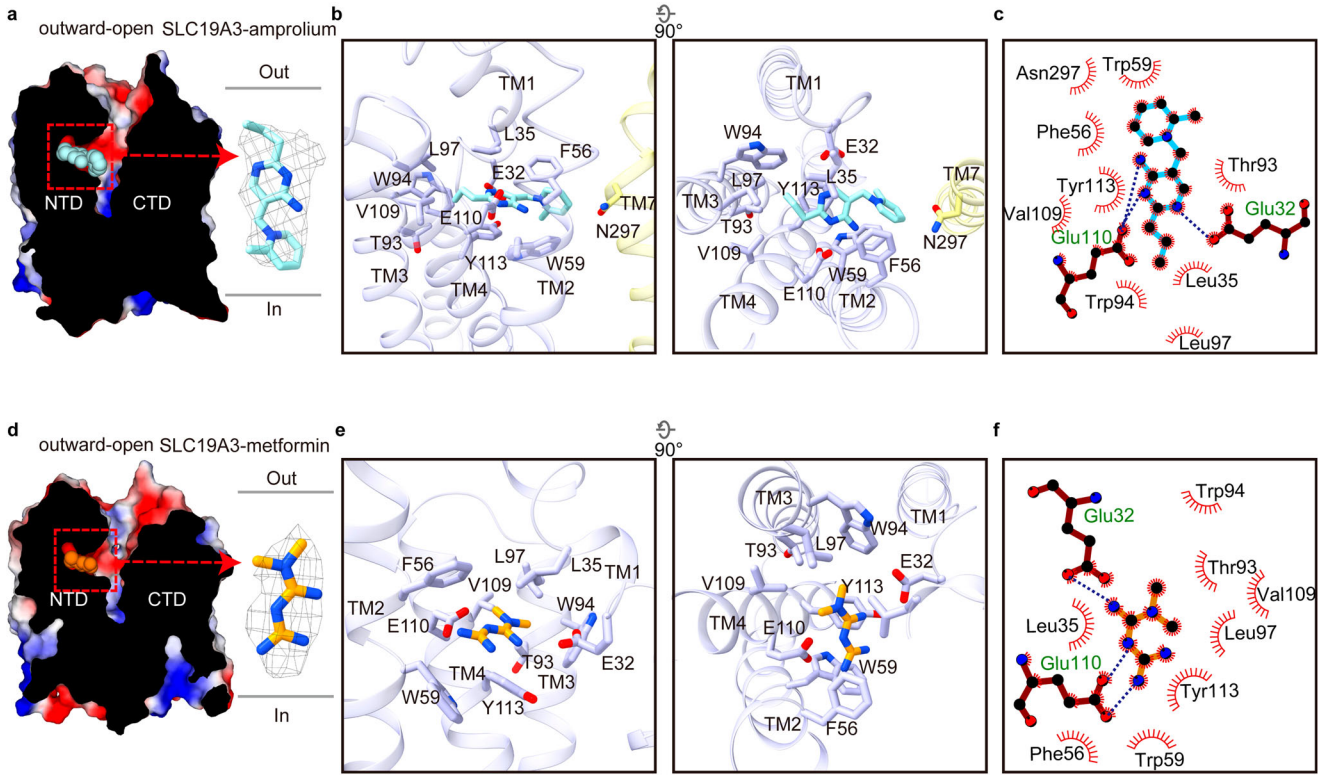

Fig. 5 | Amprolium and metformin interactions with SLC19A3. a–c Binding site of antibiotic amprolium in the outward-open SLC19A3 structure, with interaction network detailed in (**b**) and sketched in (**c**) by LIGPLOT + 1.4. Each eyelash motif indicates a hydrophobic contact. Blue dashed lines indicate hydrogen bonds between inhibitor and residues. **d–f** Localization and coordination network of metformin binding pocket in the outward-open SLC19A3 structure.

the aminopyrimidine chemical core, along with substantial conformational rearrangements observed in the outward- and inward-facing SLC19A3 structures, suggests that fedratinib inhibits SLC19A3 or SLC19A2-mediated thiamine absorption by competing for the same molecular components required for thiamine translocation. This also implies that fedratinib may be imported by thiamine transporters, warranting further investigation.

Although the driving force behind SLC19A2/A3-mediated thiamine and pyridoxine transport remains unclear, a comparison of the outward- and inward-facing SLC19A2/A3 structures reveals a rocker-switch movement that facilitates transport dynamics. In this mechanism, the pseudo-symmetric N-domain and C-domain wobble around the substrate binding pocket, which is situated near the extracellular side. Unlike the central substrate binding pockets formed by two domains seen in other MFS transporters, in the outward-open state of SLC19A2/A3, substrates-typically the aminopyrimidine group-primarily insert into the pocket on the N-domain. As the transporter transitions towards the intracellular side, a conformational rearrangement introduces an additional binding surface on the C-domain to accommodate the rest moieties of substrates. Subsequently, the substrates are released from the binding pocket into the intracellular space through an unknown force, and the transporters reset to the outward-open state to begin another cycle.

Cationic medicines like metformin and fedratinib may predispose patients to thiamine and pyridoxine deficiency, even without known risk factors. Regular assessment of plasma thiamine levels is recommended during treatment with these medications. Adequate thiamine supplementation may mitigate this overlooked disorder. Diabetic patients frequently experiencing severe lactic acidosis concurrent with thiamine deficiency while taking biguanide drugs (e.g. buformin and metformin), have shown recovery following intravenous infusion of high-dose thiamine[24,37]. Alternatively, the molecular insights into SLC19A3 inhibition by prescribed drugs elucidated in the current study, applicable to SLC19A2 as well, may aid in the future improvement of these medicines through structure-based rational design.

During the preparation of our manuscript, a preprint by Gabriel et al. presented cryo-EM structures of SLC19A3 with thiamine in outward- and inward-facing states, and several drugs including fedratinib and amprolium in inward-facing state[38]. Meanwhile, Dang et al. reported SLC19A3 bound by thiamine, pyridoxine and fedratinib in the inward-facing conformation[39]. These structures, obtained via different strategies, thus cross-validate and complement our findings regarding SLC19A3 and SLC19A2.

In conclusion, our elucidation of thiamine transporters structures in association with vitamins B_1 and B_6, and several clinical drugs, alongside biochemical evidence, offers insights into the mechanism underlying the transport of cationic vitamins and medicines. This also provides a framework for developing targeted pharmaceutical strategies.

Methods

Ethical Statement

Mouse experiments were approved by the Institutional Animal Care and Use Committees (SYXK2021070) at the Institute of Biophysics, Chinese Academy of Sciences.

SLC19A3 and SLC19A2 expression and purification

The human SLC19A3 (residues 6–472) gene (UniProt accession code: Q9BZV2) was subcloned and inserted into a pFastBac-dual vector (Invitrogen), followed by a TEV site and a C-terminal 11×His tag. The corresponding construct and primer sequences are listed in the Supplementary Data file. SLC19A3 was expressed in Spodoptera frugiperda Sf9 cells. Cells were infected at a density of 2.5-3 × 10^6 cells per ml. After growing for 72 h at 27 °C, cells were collected and

resuspended in buffer containing 50 mM Tris-HCl pH 7.5, 300 mM NaCl, 20 mM imidazole. Then cells were disrupted by sonication and solubilized with 1% (w/v) n-dodecyl-b-d-maltoside (DDM, Anatrace) at 4 °C for 1.5 h. After centrifugation (30,000 xg, 30 min, 4 °C), the supernatant was incubated with nickel affinity resin at 4 °C for 1 h. The resin was then washed with buffer containing 50 mM Tris-HCl pH 7.5, 300 mM NaCl, 40 mM imidazole, and 0.025% (w/v) n-dodecyl-b-D-maltoside (DDM, Anatrace). The human SLC19A3 protein was eluted with 50 mM Tris pH 7.5, 300 mM NaCl, 500 mM imidazole, 0.025%(w/v) DDM. Then the protein was concentrated and loaded onto a Superdex 200 Increase 10/300 GL size-exclusion column (GE Healthcare) in the presence of 20 mM HEPES pH 7.5, 150 mM NaCl, 0.025% (w/v) DDM. The peak fractions were concentrated to about 10 mg/ml.

Human SLC19A3 lacking the N-terminal 12 residues was modified with an N-terminal MPER(LWNWFDITNWLWYIKSL) and cloned into the pcDNA3.1 vector. SLC19A3 was expressed in HEK293 cells. Cells were infected at a density of 2×10^6 cells per ml and 10 mM sodium butyrate was added. Cells overexpressed SLC19A3 were collected 58 h after infection and were re-suspended in buffer A (50 mM HEPES, pH 7.5, 150 mM NaCl, 5% glycerol, and 1 × protease inhibitor cocktail). The re-suspended cells were lysed mechanically with a Dounce tissue grinder and agitated at 4 °C for 3 h in lysis buffer containing 1% LMNG, and 0.1% CHS. After agitation, the supernatant was collected after centrifugation at 30,000 × g at 4 °C for 40 min and incubated with anti-Strep affinity resin by agitation for 3 h. Then the resin was collected on a gravity column and the supernatant was incubated with new anti-Strep affinity resin by agitation for 3 h. Then, the resin was washed with 10 column volume (CV) of buffer B (buffer A supplemented with 0.1% LMNG, 0.01% CHS), buffer C (buffer A supplemented with 0.01% LMNG, 0.001% CHS), buffer D (buffer A supplemented with 0.001% LMNG, 0.0001% CHS). SLC19A3 was eluted with buffer E (buffer A supplemented with 2.5 mM D-Desthiobiotin). The elution was added to Fab_10E8v4 in a ratio of 1:10 and concentrated then further purified by size-exclusion chromatography on a Superose6 10/300 GL column (GE Healthcare) in buffer containing 0.001% LMNG, 0.0001% CHS, 50 mM HEPES, pH 7.5, and 150 mM NaCl. For the Thiamine sample, Thiamine (Sigma Aldrich) was added at a concentration of 2.5 mM to the SEC buffer (50 mM MES, pH 6.0, and 150 mM NaCl, 0.001% LMNG, 0.0001% CHS). The peak fractions were concentrated to 14.5 mg/ml for grid preparation.

Human SLC19A2 lacking the N-terminal 30 residues was modified with an N-terminal MPER tag and cloned into the pcDNA3.1 vector. The expression and purification of SLC19A2 were carried out similarly as described above with SLC19A3.

Antibody generation

All the mice used in this study are BALB/c background female mice and maintained in a specific-pathogen-free facility (temperature 20-22 °C, humidity 50-60%, 12 h light–dark cycle). All mice were used at age of 6-20 weeks.

The BALB/c mice female were immunized monthly with human SLC19A3 (residues 6-472) plus Mn2+ adjuvant (MnStarter Biotechnology) and CpG1826 (Thermo Fisher Scientific). Sera from the immunized mice were analyzed for reactivity towards human SLC19A3-expressing HEK293T cells using flow cytometry. Hybridoma formation was conducted following our previously established protocols[40]. Briefly, three days post final boost immunization (without adjuvant), spleen and lymph node cells from the immunized mice were isolated and fused with SP2/0 myeloma cells using 50% polyethylene glycol (PEG) 4000 (Sigma-Aldrich). Subsequently, the cells were plated in 96-well plates containing Hypoxanthine/Aminopterin/Thymidine (HAT) medium (Sigma-Aldrich) with feeder cells (peritoneal macrophages) that had been seeded 24 h earlier. The hybridoma culture supernatants were screened using flow cytometry with human SLC19A3 and human SLC19A3 (6/7 loop replaced with GSGSGSGSGS) expressing HEK293T cells on an Attune NxT Flow Cytometer (Thermo Fisher Scientific). Double positive hybridomas were subcloned, after 7 days, the subcloned supernatants were analyzed. The double positive clones were then collected, barcoded using the 10x Chromium Single Cell platform (10x Genomics), and 17 recombinant monoclonal antibodies against SLC19A3 were synthesized using established methods[27]. BCR sequences were assembled and evaluated using the V(D)J tool of Cell Ranger suit (v.6.0.1) against the GRCm38 reference genome with specific parameters. Contigs labeled as low-confidence, non-productive or with UMIs <2 were excluded. Only cells containing at least one light chain (IGL) and one heavy chain (IGH) were remained. In each filtered B cell, light and heavy chains were paired and ranked based on their mean clone levels. The selected V(D)J sequences of IGL and IGH were synthesized and cloned into vectors containing the myc-tagged heavy chain constant regions 1 (CH1) of mouse IgG2a or κ light chain respectively. The antibodies were produced in 293 F Human Embryonic Kidney cells and purified with a protein A agarose pre-packed column. The binding of the purified antibodies to SLC19A3 and its truncations was confirmed by FACS.

Fab expression and purification

The DNA sequences of the heavy and light chains of MPER - bound Fab_10E8v4 (McIlwain BC, et al. 2021, *J Mol Biol.*) were cloned into pDEC vectors separately. 2 mg plasmid of Fab (including 1 mg heavy and 1 mg light chains) and 4 mg of PEI were mixed in 100 mL of medium for 15 min at RT before being added into 1 L of cell culture at a density of 2×10^6 ml^{-1}, containing 10 mM sodium butyrate. After 48 h, the cell culture media was centrifuged at 2000 xg for 15 min, and then the supernatant was filtered and exchanged into buffer F (50 mM Tris, pH 8.0, 150 mM NaCl, 5% glycerol). Then, the supernatant was incubated with Ni beads by agitation for 3 h, and the beads were washed with 20 CV of buffer F containing 20 mM imidazole. Fab_10E8v4 was eluted with buffer F with the addition of 300 mM imidazole. The elution was concentrated to high concentration and stored at −80 °C. SLC19A3-bound Fabs were expressed and purified similarly as Fab_10E8v4.

Assembly of SLC19A3-Fab complexes in detergent micells and nanodisc

For the SLC19A3-Fab complex in detergent micells, SLC19A3 was incubated with fab at a molar ratio of 1:1.1 for 1 h and the mixture was loaded onto the Superdex 200 Increase 10/300 GL size-exclusion column and eluted with buffer containing 20 mM HEPES pH 7.5, 150 mM NaCl and 0.025%(w/v) DDM. Peak fractions containing SLC19A3–Fab complexes were concentrated to about 12 mg/ml. For nanodisc reconstitution, SLC19A3 was mixed with membrane scaffold protein MSP1D1 and POPG (Avanti) at a molar ratio of 1:1.9:84 and incubated at 4 °C with constant rotation for 1 h. Subsequently, Bio-beads were added to the mixture at 100 mg/ml to remove detergent at 4 °C overnight with gentle agitation. The Bio-beads were removed and the nanodisc reconstitution mixture was incubated with fab at a molar ratio of 1:1.1 for 1 h. Then the mixture was loaded onto the Superdex 200 Increase 10/300 GL size-exclusion column and eluted with buffer containing 20 mM HEPES pH 7.5 and 150 mM NaCl. Peak fractions corresponding to nanodisc-reconstituted SLC19A3–Fab complexes were concentrated to about 12 mg/ml.

Cryo-EM sample preparation and data collection

Quantifoil Au 1.2/1.3 (300 mesh) grids were glow-discharged 10 mA for 50 s in an PELCO easiGlo instrument. 2.5 μL protein samples were deposited on the grids and blotted for 4 s with filter paper at 4 °C and 100% humidity using Vitrobot (FEI) equipment and vitrified in liquid ethane at liquid nitrogen temperature. The frozen grids were transferred under cryogenic conditions and stored in liquid nitrogen for subsequent screening and cryo-EM data collection. To prepare the substrate-bound SLC19A3 samples, 100 μM fedratinib was incubated

with the MPER-SLC19A3/Fab_10E8v4 complex on ice for 1 h. For the cryo-EM sample of SLC19A2 bonded pyridoxine, 200 μM pyridoxine was incubated with the MPER-SLC19A2/Fab_10E8v4 complex on ice for 1 h. To improve particle distribution, 0.035 mM fluorinated octyl maltoside was added to all cryo-EM samples. All datasets were collected on Titan Krios G4 cryo-electron microscope operated at 300 kV, equipped with a Falcon G4i direct electron detector with a Selectris X imaging filter (ThermoFisher Scientific), operated with a 20-eV slit size. Movie stacks were acquired using the EPU software (ThermoFisher Scientific) in super-resolution mode with a defocus range of −1.2 to −2.0 μm and a final calibrated pixel size of 0.932 Å. The total dose per EER (electron event representation) movie was 50 $e^-/Å^2$.

For the SLC19A3-thiamine/pyridoxine/metformin samples, the purified SLC19A3–Fab complexes in detergent micells were concentrated to about 12 mg/ml and separately incubated with 5 mM thiamine (Sigma-Aldrich), 5 mM pyridoxine (Sigma-Aldrich) or 5 mM metformin (Sigma-Aldrich) for 1 h before being applied to the grids. For fedratinib/amprolium-bound samples, the purified nanodisc-reconstituted SLC19A3–Fab complexes were separately incubated with 1 mM fedratinib (Sigma-Aldrich) or 5 mM amprolium (Sigma-Aldrich) for 1 h before cryo-EM sample preparation. In brief, 3 μl of the purified SLC19A3-ligand complexes in detergent micelles or nanodiscs was added to glow-discharged holey grids (Au R1.2/1.3, 300 mesh Quantifoil). The grids were blotted for 3-4 s at 4 °C with 100% humidity, and then plunge-frozen into liquid ethane. The cryo-EM data for SLC19A3-amprolium sample were collected using a Titan Krios electron microscope (Thermo Fisher Scientific) equipped with a BioQuantum GIF energy filter with a K2 summit direct detector (Gatan). Other cryo-EM datasets were collected using SerialEM[41] on the Talos Arctica 200 kV FEG (Thermo Fisher Scientific) with a K2 summit direct electron elector (Gatan) and a GIF quantum energy filter (Gatan). All movie stacks were automatically acquired at a magnification of 130,000× under superresolution mode. The slit width was set to 20 eV. The total dose was 60 e $Å^{-2}$ with a dose rate of 9.2 $e^- Å^{-2}$ s. Each video was fractionated into 32 frames. The defocus range was set between −1.2 and −1.5 μm. The pixel size was calibrated at 0.5 Å (×130,000) under super-resolution mode. Images were recorded using beam–image shift data collection methods[4].

Cryo-EM data processing

For the outward-open SLC19A3-apo/thiamine/pyridoxine/fedratinib/amprolium/metformin structure dataset, 914, 2465, 1445, 2227, and 2152 super-resolution movie stacks were aligned, summed and dose-weighted using the program MotionCor2[42], and then imported into cryoSPARC[43]. The processing of the outward-open SLC19A3-apo/thiamine/ pyridoxine/ fedratinib/ amprolium/ metformin structure analysis adopted a similar scheme of classification and refinement; therefore, the detailed procedures were introduced with SLC19A3-thiamine dataset processing as example (Supplementary Fig. 3). The processing of the other datasets was illustrated in flowchart (Supplementary Figs. 4,5). All datasets were similarly processed in cryoSPARC (v.4.2.1) and RELION (v.3.1.4)[44].

For the inward-open SLC19A2 and SLC19A3 structures, all datasets were similarly processed in cryoSPARC (v.3.3.2) and RELION (v.3.1.4). Briefly, each 1080-frame EER movie was divided into 40 subgroups, and beam-induced motion was corrected using a MotionCor2-like algorithm implemented in RELION. Exposure-weighted micrographs were then imported into cryoSPARC for CTF (contrast transfer function) estimation by patch CTF. Particles were blob-picked and extracted and multiple rounds of 2D classification were performed. Multiple rounds of heterogeneous refinement (3D classification) were performed using ab initio reference maps reconstructed with good 2D averages. The good particles were then converted to Bayesian polishing in RELION and imported back into cryoSPARC. Final maps were obtained by local refinement on the transmembrane domain of SLC19A3. The resolution of these maps was estimated internally in cryoSPARC by gold standard Fourier shell correlation using the 0.143 criterion.

Model building and refinement

For the atomic model of apo SLC19A3, the structure of SLC19A3 (ID: AF-Q9BZV2-F1) predicted by AlphaFold[45], as the initial model, was manual fitted in UCSF Chimera[46] and checked in COOT[47]. The corrected model was further refined by real space refinement in PHENIX[48]. CIF files for ligands were generated in PHENIX using eLBOW[49]. In COOT and PHENIX, with the apo SLC19A3 as the initial model, the atomic model of ligand-bound SLC19A3 was generated by several rounds of real space refinement. Thiamine, or pyridoxine, or fedratinib, or amprolium, or metformin was fitted into the density using COOT. The resulting model was then manually rebuilt in COOT and further refined by real space refinement in PHENIX. The model stereochemistry was evaluated using the comprehensive validation (cryo-EM) utility in PHENIX. The final refinement statistics are provided in Supplementary Table 1. All figures were prepared with UCSF ChimeraX[50] or Pymol (PyMOL Molecular Graphics SYtem, v.2.3.4, Scöhrödinger) (https://pymol.org/2/).

Generation of stable cell lines overexpressing SLC19A2/SLC19A3 and mutants

The DNA sequences encoding human SLC19A2/SLC19A3 and responsive mutants were cloned into a lentiviral plasmid. This lentiviral plasmid co-expressed the reporter gene mcherry through a P2A sequence controlled by the human EEF1A1 promoter. For lentiviral gene transduction, HEK293T cells were transfected with the respective lentiviral vectors and packaging plasmids σNRF and vesicular stomatitis virus G (an envelope plasmid) using standard calcium phosphate techniques. After 48 h, culture supernatants were collected, filtered through 0.45-μm polyethersulfone filters (Merck Millipore) and supplemented with 8 μg/ml polybrene (Sigma-Aldrich). Cells were infected by spinfection (2000 xg, 180 min, room temperature). Following 72 h of culture, lentiviral-infected cells expressing comparable levels of mcherry were isolated using a BD FACSAria III cell sorter (BD Biosciences) after gating on single cells.

[^{3}H]-Thiamine cellular uptake assay

Stably expressing either wild type or mutated SLC19A3 or SLC19A2 293 T cells were seeded into poly-lysine-coated 24-well plates at 1 ×10^5 cells per well and grown for 12 h. Cells were firstly washed once with 0.5 ml HBSS buffer at pH 7.4 and then incubated in HBSS buffer at 37°C for 10 min. Subsequently, 0.2 ml HBSS buffer containing 5 nM [^{3}H]-thiamine (American Radiolabeled Chemicals) was used to replace the cell medium to initiate the uptake assay. After 3 min, cells were washed twice with 0.5 ml ice-cold HBSS buffer, and then lysed with 0.2 ml 0.2 M NaOH for 5 min. The amount of [^{3}H]-thiamine was calculated by and indicated concentration of inhibitors was used to initiate the uptake. All datasets were analyzed using GraphPad Prism 9 (https://www.graphpad.com/).

Microscale thermophoresis assay

Binding of SLC19A2 and SLC19A3 to thiamine, pyridoxine, fedratinib, erythromycin, thiamine pyrophosphate, metformin, amprolium were measured by MST experiment. The eGFP-tagged full-length SLC19A2 and SLC19A3 were purified by size exclusion chromatography in the assay buffer (50 mM MES pH 6.0,150 mM NaCl, 0.01% DDM, 0.001% CHS). Peak fractions were pooled and diluted to 40 nM. Ligand stocks (250 mM thiamine, 200 mM pyridoxine, 125 mM fedratinib, 100 mM erythromycin, 90 mM thiamine pyrophosphate, 200 mM metformin, 600 mM amprolium) were diluted to a suitable concentration used in the assay buffer. For MST measurements, a series of 16 sequential 1:1 dilutions were prepared

using assay buffer for each ligand, and each ligand dilution was mixed 1:1 with diluted protein to final protein concentration of 20 nM and final ligand concentrations in the µM to nM range. The samples were incubated for 10 min at room temperature, and then loaded into Standard Monolith Capillaries (Cat# MO-K022, NanoTemper Technologies). Measurements were carried out with a Monolith NT.115 device at 80% LED power and 40% MST power. *K*d was determined using the MO. Affinity Analysis software (version 2.3, NanoTemper Technologies, Germany) is with the *K*d fit function. Capillaries displaying aggregation or adsorption were excluded. Data of at least three independently pipetted measurements were analyzed and *K*d is expressed as mean ± SEM. Binding curves were plotted by GraphPad Prism Prism 9.5.1 (GraphPad Software Inc., San Diego, USA).

In silico molecular docking

Structures of human SLC19A3 and SLC19A2 in an inward/outward-open conformation were prepared in Schrödinger (Release 2021-2) for docking. SLC19A3 in an inward-open conformation was obtained by homologous modeling SLC19A2-pyridoxine as template, and SLC19A2 in an outward-open conformation was obtained by homologous modeling SLC19A3-thiamine/pyridoxine as template. Prime (Schrödinger) was used to complete the missing side-chains and to cap the chain termini. After removal of the ligand, the protonation states and tautomers were assigned at pH 6.0/7.5 ± 2 using Epik[51] in Maestro with the OPLS3 forcefield[52]. The docking grid was centered around the binding site, with the ligand diameter midpoint box of 25 Å on all three axes. Docking is run with the Glide standard precision (SP) scoring function[53].

Molecular dynamics simulations

We performed all-atom molecular dynamics (MD) simulations in explicit solvents for nine protein-ligand complexes, SLC19A3-thiamine/pyridoxine/fedratinib/amprolium/metformin and SLC19A2-thiamine/pyridoxine in an inward/outward-open conformation. The chain termini were neutralized by capping groups (acetylation and methylation) to avoid termini-charge dependent effects. PropKa was used to determine the dominant protonation state of all titratable residues at pH 6.0/7.4[54]. The CHARMM-GUI Membrane builder module[55] was used to place each protein in a 1:1 POPC membrane patch with 20 Å of water above and below and 0.15 M NaCl in the solution. The final systems had ~126 POPC lipids, ~14,570 water molecules, and initial dimensions of 80 × 80 × 117 Å3. The CHARMM36m force field was adopted for lipids, proteins, sodium and chloride ions, and the TIP3P model for waters[56]. Ligands were modeled with the CHARMM CGenFF small-molecule force field.

Simulations were performed using Gromacs 2020. 7[57]. For each condition, three independent simulations were run. All systems were energy minimized and equilibrated in six steps consisting of 2.5 ns long simulations, while slowly releasing the position restrain forces acting on the Cα atoms. Initial random velocities were assigned independently to each system. Production simulations were performed for 200 ns. The Verlet neighbor list was updated every 20 steps with a cutoff of 12 Å and a buffer tolerance of 0.005 kJ/mol/ps. Non-bonded van der Waals interactions were truncated between 10 and 12 Å using a force-based switching method. Long-range electrostatic interactions under periodic boundary conditions were evaluated by using the smooth particle mesh Ewald method with a real-space cutoff of 12 Å[58]. Bonds to hydrogen atoms were constrained with the P-LINCS algorithm with an expansion order of four and one LINCS iteration[59]. The constant temperature was maintained at 310 K using the v-rescale (τ = 0.1 ps) thermostat[60] by separately coupling solvent plus salt ions, membrane, and protein. Semi-isotropic pressure coupling was applied using the Parrinello-Rahman barostat, using 1 bar and applying a coupling constant of 1 ps. Finally, a restraint-free production run was carried out for each simulation, with a time step of 2 fs.

MM/GBSA calculations

Molecular mechanics with generalized Born and surface area solvation (MM/GBSA) is a widely used approach for determining the free energy associated with the binding of ligands to proteins, and it has been demonstrated to balance precision with computational efficiency, particularly when working with large systems[61]. Free energy calculations were performed with gmx MMPBSA using Gromacs trajectory and topology files[62,63]. The total binding energy (ΔTOTAL) for each complex is contributed by the different components, including van der Waals (ΔVDWAALS), electrostatic energy (ΔEEL), polar solvation energy in Poisson–Boltzmann methods (ΔEPB), non-polar solvation energy in Poisson–Boltzmann methods (ΔENPOLAR), gas-phase molecular mechanics free energy (ΔGGAS) and solvation free energy (ΔGSOLV). Based on the results of the ligand RMSD, the MDS trajectories with the 50 ns period that ligand binding stably were selected for the MM/PBSA analysis.

Reporting summary

Further information on research design is available in the Nature Portfolio Reporting Summary linked to this article.

Data availability

The data that support this study are available from the corresponding authors upon request. The cryo-EM maps have been deposited into the Electron Microscopy Data bank under accession numbers: EMD-39825 (SLC19A3 apo outward), EMD-39826 (SLC19A3-thiamine outward), EMD-39827 (SLC19A3-pyridoxine outward), EMD-39828 (SLC19A3-fedratinib outward), EMD-39829 (SLC19A3-amprolium outward), EMD-39830 (SLC19A3-metformin outward), EMD-39831 (SLC19A3-thiamine inward), EMD-39832 (SLC19A3-fedratinib inward), EMD-39833 (SLC19A2-thiamine inward) and EMD-39834 (SLC19A2-pyridoxine inward). The coordinates have been deposited at the Protein Data Bank under accession numbers: 8Z7R (SLC19A3 apo outward), 8Z7S (SLC19A3-thiamine outward), 8Z7T (SLC19A3-pyridoxine outward), 8Z7U (SLC19A3-fedratinib outward), 8Z7V (SLC19A3-amprolium outward), 8Z7W (SLC19A3-metformin outward), 8Z7X (SLC19A3-thiamine inward), 8Z7Y (SLC19A3-fedratinib inward), 8Z7Z (SLC19A2-thiamine inward) and 8Z80 (SLC19A2-pyridoxine inward). A source Data file is included with this manuscript. Initial and final MD simulation trajectories can be found in the Source Data file. Source data are provided with this paper.

References

1. Institute of Medicine (US) Standing Committee on the Scientific Evaluation of Dietary Reference Intakes and its Panel on Folate, Other B Vitamins, and Choline. *Dietary Reference Intakes for Thiamin, Riboflavin, Niacin, Vitamin B6, Folate, Vitamin B12, Pantothenic Acid, Biotin, and Choline*. (National Academies Press (US), Washington (DC), 1998).
2. Brown, G. & Plecko, B. Disorders of Thiamine and Pyridoxine Metabolism. in *Inborn Metabolic Diseases: Diagnosis and Treatment* (eds. Saudubray, J.-M., Baumgartner, M. R., García-Cazorla, Á. & Walter, J.) 531–545 (Springer, Berlin, Heidelberg, 2022). https://doi.org/10.1007/978-3-662-63123-2_29.
3. Fattal-Valevski, A. Thiamine (Vitamin B1). *J. Evid. -Based Complement. Altern. Med.* **16**, 12–20 (2011).
4. Calderón-Ospina, C. A. & Nava-Mesa, M. O. B Vitamins in the nervous system: Current knowledge of the biochemical modes of action and synergies of thiamine, pyridoxine, and cobalamin. *CNS Neurosci. Ther.* **26**, 5–13 (2020).

5. Dutta, B. et al. Cloning of the human thiamine transporter, a member of the folate transporter. *Fam. *. J. Biol. Chem.* **274**, 31925–31929 (1999).
6. Rajgopal, A., Edmondnson, A., Goldman, I. D. & Zhao, R. SLC19A3 encodes a second thiamine transporter ThTr2. *Biochim. Biophys. Acta* **1537**, 175–178 (2001).
7. Yamashiro, T., Yasujima, T., Said, H. M. & Yuasa, H. pH-dependent pyridoxine transport by SLC19A2 and SLC19A3: Implications for absorption in acidic microclimates. *J. Biol. Chem.* **295**, 16998–17008 (2020).
8. Eudy, J. D. et al. Identification and characterization of the human and mouse SLC19A3 gene: a novel member of the reduced folate family of micronutrient transporter genes. *Mol. Genet. Metab.* **71**, 581–590 (2000).
9. Labay, V. et al. Mutations in SLC19A2 cause thiamine-responsive megaloblastic anaemia associated with diabetes mellitus and deafness. *Nat. Genet.* **22**, 300–304 (1999).
10. Oishi, K. et al. Targeted disruption of Slc19a2, the gene encoding the high-affinity thiamin transporter Thtr-1, causes diabetes mellitus, sensorineural deafness and megaloblastosis in mice. *Hum. Mol. Genet.* **11**, 2951–2960 (2002).
11. Kono, S. et al. Mutations in a thiamine-transporter gene and Wernicke's-like encephalopathy. *N. Engl. J. Med.* **360**, 1792–1794 (2009).
12. Wang, J. et al. Report of the largest Chinese Cohort With SLC19A3 gene defect and literature review. *Front. Genet.* **12**, 683255 (2021).
13. Alfadhel, M. et al. Targeted SLC19A3 gene sequencing of 3000 Saudi newborn: a pilot study toward newborn screening. *Ann. Clin. Transl. Neurol.* **6**, 2097–2103 (2019).
14. Zeng, W.-Q. et al. Biotin-responsive Basal Ganglia Disease Maps to 2q36.3 and is due to mutations in *SLC19A3*. *Am. J. Hum. Genet.* **77**, 16–26 (2005).
15. Reidling, J. C., Lambrecht, N., Kassir, M. & Said, H. M. Impaired Intestinal Vitamin B1 (Thiamin) uptake in Thiamin Transporter-2–deficient mice. *Gastroenterology* **138**, 1802–1809 (2010).
16. Wen, A. et al. The impacts of Slc19a3 deletion and intestinal SLC19A3 insertion on Thiamine distribution and brain metabolism in the mouse. *Metabolites* **13**, 885 (2023).
17. Neufeld, E. J., Fleming, J. C., Tartaglini, E. & Steinkamp, M. P. Thiamine-responsive megaloblastic anemia syndrome: a disorder of high-affinity thiamine transport. *Blood Cells Mol. Dis.* **27**, 135–138 (2001).
18. Chen, L. et al. OCT1 is a high-capacity thiamine transporter that regulates hepatic steatosis and is a target of metformin. *Proc. Natl Acad. Sci.* **111**, 9983–9988 (2014).
19. Liang, X. et al. Metformin Is a substrate and inhibitor of the human thiamine Transporter, THTR-2 (SLC19A3). *Mol. Pharm.* **12**, 4301–4310 (2015).
20. Zhang, Q. et al. The Janus Kinase 2 Inhibitor Fedratinib inhibits Thiamine uptake: a putative mechanism for the onset of Wernicke's Encephalopathy. *Drug Metab. Dispos.* **42**, 1656–1662 (2014).
21. Vora, B. et al. Drug–nutrient interactions: discovering prescription drug inhibitors of the thiamine transporter ThTR-2 (SLC19A3). *Am. J. Clin. Nutr.* **111**, 110–121 (2020).
22. Giacomini, M. M. et al. Interaction of 2,4-Diaminopyrimidine-containing drugs including Fedratinib and Trimethoprim with Thiamine transporters. *Drug Metab. Dispos. Biol. Fate Chem.* **45**, 76–85 (2017).
23. McGarvey, C., Franconi, C., Prentice, D. & Bynevelt, M. Metformin-induced encephalopathy: the role of thiamine. *Intern. Med. J.* **48**, 194–197 (2018).
24. Ziegler, D., Reiners, K., Strom, A. & Obeid, R. Association between diabetes and thiamine status - A systematic review and meta-analysis. *Metab Clin. Exp.* **144**, 155565 (2023).
25. Drew, D., North, R. A., Nagarathinam, K. & Tanabe, M. Structures and general transport mechanisms by the Major Facilitator Superfamily (MFS). *Chem. Rev.* **121**, 5289–5335 (2021).
26. Yan, N. Structural biology of the major facilitator superfamily transporters. *Annu. Rev. Biophys.* **44**, 257–283 (2015).
27. Zhang, Q. et al. Recognition of cyclic dinucleotides and folates by human SLC19A1. *Nature* **612**, 170–176 (2022).
28. Wright, N. J. et al. Methotrexate recognition by the human reduced folate carrier SLC19A1. *Nature* **609**, 1056–1062 (2022).
29. Dang, Y. et al. Molecular mechanism of substrate recognition by folate transporter SLC19A1. *Cell Discov.* **8**, 1–11 (2022).
30. McIlwain, B. C. et al. N-terminal Transmembrane-Helix Epitope Tag for X-ray crystallography and electron microscopy of small membrane proteins. *J. Mol. Biol.* **433**, 166909 (2021).
31. Subramanian, V. S., Marchant, J. S., Parker, I. & Said, H. M. Cell Biology of the Human Thiamine Transporter-1 (hTHTR1): Intracellular trafficking and membrane targeting mechanisms * 210. *J. Biol. Chem.* **278**, 3976–3984 (2003).
32. Blair, H. A. Fedratinib: First approval. *Drugs* **79**, 1719–1725 (2019).
33. Meyer, M. J. et al. Differences in Metformin and Thiamine uptake between human and mouse organic Cation Transporter 1: Structural determinants and potential consequences for intrahepatic concentrations. *Drug Metab. Dispos.* **48**, 1380–1392 (2020).
34. Zeng, Y. C. et al. Structural basis of promiscuous substrate transport by Organic Cation Transporter 1. *Nat. Commun.* **14**, 6374 (2023).
35. Dudeja, P. K., Tyagi, S., Kavilaveettil, R. J., Gill, R. & Said, H. M. Mechanism of thiamine uptake by human jejunal brush-border membrane vesicles. *Am. J. Physiol. Cell Physiol.* **281**, C786–C792 (2001).
36. Wesół-Kucharska, D. et al. Early treatment of biotin–thiamine–responsive basal ganglia disease improves the prognosis. *Mol. Genet. Metab. Rep.* **29**, 100801 (2021).
37. Godo, S. et al. The dramatic recovery of a patient with biguanide-associated severe lactic acidosis following thiamine supplementation. *Intern. Med.* **56**, 455–459 (2017).
38. Gabriel, F. et al. Structural basis of substrate transport and drug recognition by the human thiamine transporter SLC19A3. *Nat. Commun.* **15**, 8542 (2024).
39. Dang, Y. et al. Substrate and drug recognition mechanisms of SLC19A3. *Cell Res.* 1–4 https://doi.org/10.1038/s41422-024-00951-2 (2024).
40. Zhang, X. et al. The binding of a monoclonal antibody to the apical region of SCARB2 blocks EV71 infection. *Protein Cell* **8**, 590–600 (2017).
41. Mastronarde, D. N. Automated electron microscope tomography using robust prediction of specimen movements. *J. Struct. Biol.* **152**, 36–51 (2005).
42. Zheng, S. Q. et al. MotionCor2: anisotropic correction of beam-induced motion for improved cryo-electron microscopy. *Nat. Methods* **14**, 331–332 (2017).
43. Punjani, A., Rubinstein, J. L., Fleet, D. J. & Brubaker, M. A. cryoSPARC: algorithms for rapid unsupervised cryo-EM structure determination. *Nat. Methods* **14**, 290–296 (2017).
44. Zivanov, J. et al. New tools for automated high-resolution cryo-EM structure determination in RELION-3. *eLife* **7**, e42166 (2018).
45. Jumper, J. et al. Highly accurate protein structure prediction with AlphaFold. *Nature* **596**, 583–589 (2021).
46. Ef, P. et al. UCSF Chimera--a visualization system for exploratory research and analysis. *J. Comput. Chem.* **25** https://pubmed.ncbi.nlm.nih.gov/15264254/ (2004).
47. Emsley, P., Lohkamp, B., Scott, W. G. & Cowtan, K. Features and development of Coot. *Acta Crystallogr. D. Biol. Crystallogr.* **66**, 486–501 (2010).
48. Adams, P. D. et al. PHENIX: a comprehensive Python-based system for macromolecular structure solution. *Acta Crystallogr. D Biol. Crystallogr.* **66**, 213–221 (2010).

49. Moriarty, N. W., Grosse-Kunstleve, R. W. & Adams, P. D. electronic Ligand Builder and Optimization Workbench (eLBOW): a tool for ligand coordinate and restraint generation. *Acta Crystallogr. D. Biol. Crystallogr.* **65**, 1074–1080 (2009).
50. Goddard, T. D. et al. UCSF ChimeraX: Meeting modern challenges in visualization and analysis. *Protein Sci. Publ. Protein Soc.* **27**, 14–25 (2018).
51. Shelley, J. C. et al. Epik: a software program for pKaprediction and protonation state generation for drug-like molecules. *J. Comput. Aided Mol. Des.* **21**, 681–691 (2007).
52. Harder, E. et al. OPLS3: A force field providing broad coverage of drug-like small molecules and proteins. *J. Chem. Theory Comput.* **12**, 281–296 (2016).
53. Halgren, T. A. et al. Glide: A new approach for rapid, accurate docking and scoring. 2. Enrichment factors in database screening. *J. Med. Chem.* **47**, 1750–1759 (2004).
54. Olsson, M. H. M., Søndergaard, C. R., Rostkowski, M. & Jensen, J. H. PROPKA3: Consistent treatment of internal and surface residues in empirical pKa predictions. *J. Chem. Theory Comput.* **7**, 525–537 (2011).
55. Wu, E. L. et al. CHARMM-GUI Membrane Builder toward realistic biological membrane simulations. *J. Comput. Chem.* **35**, 1997–2004 (2014).
56. Huang, J. et al. CHARMM36m: an improved force field for folded and intrinsically disordered proteins. *Nat. Methods* **14**, 71–73 (2017).
57. Abraham, M. J. et al. GROMACS: High performance molecular simulations through multi-level parallelism from laptops to supercomputers. *SoftwareX* **1**, 19–25 (2015).
58. Steinbach, P. J. & Brooks, B. R. New spherical-cutoff methods for long-range forces in macromolecular simulation. *J. Comput. Chem.* **15**, 667–683 (1994).
59. Hess, B. P-LINCS: A parallel linear constraint solver for molecular simulation. *J. Chem. Theory Comput.* **4**, 116–122 (2008).
60. Bussi, G., Donadio, D. & Parrinello, M. Canonical sampling through velocity rescaling. *J. Chem. Phys.* **126**, 014101 (2007).
61. Godschalk, F., Genheden, S., Söderhjelm, P. & Ryde, U. Comparison of MM/GBSA calculations based on explicit and implicit solvent simulations. *Phys. Chem. Chem. Phys.* **15**, 7731–7739 (2013).
62. Valdés-Tresanco, M. S., Valdés-Tresanco, M. E., Valiente, P. A. & Moreno, E. gmx_MMPBSA: A new tool to perform end-state free energy calculations with GROMACS. *J. Chem. Theory Comput.* https://doi.org/10.1021/acs.jctc.1c00645 (2021).
63. Bill R. Miller, I. I. I. et al. MMPBSA.py: An Efficient Program for End-State Free Energy Calculations. *ACS Publications* https://pubs.acs.org/doi/abs/10.1021/ct300418h (2012).

Acknowledgements

We thank the staff members of the Center of Cryo-EM, Core Facility of Shanghai Medical College, Fudan University, the Center for Biological Imaging, Core Facilities for Protein Science at the Institute of Biophysics, Chinese Academy of Sciences for technical support and assistance. All radioactivity experiments were performed at the Radioactive Isotope Laboratory (Institute of Biophysics, CAS), with guidance from H. J. Zhang in handling radioactive materials. This work has been supported by the National Key R&D Program of China (2023YFA0915000 to Q.Q.), the National Natural Science Foundation of China (32171194 & 32371256 to Q.Q.; 32325028 & 32130057 to P.G.; 32071200 to Y.W.), National Science and Technology Major Project of China (2023ZD0503203 to Q.Q.), Beijing Natural Science Foundation (Z220018 to P.G.), CAS Project for Young Scientists in Basic Research (YSBR-074 to P.G.), Strategic Priority Research Program at the Chinese Academy of Sciences (XDB37030203 to P.G.).

Author contributions

P.G., Q.Q. and L.Z. initiated and oversaw the project. P.L., Z.Zhu and Y.W. purified protein, prepared cryo-EM samples and collected cryo-EM data, with assistance of Y.C., Z.Zhou. and Y.Long. P.L., Y.W. and Q.Q. processed the cryo-EM data and reconstructed density maps. Y.W., P.G., Y.G. and Z.Zhou built and refined models. C.Y. performed MD simulations. X.Z., Y.Z., and P.L. performed antibody screening and validation. S.L. assisted with cell culture and protein expression. Z.Zhu performed biochemical assays. Y.W., X.Z., and P.L. performed cellular assays. Q.Q., P.G., P.L., Z.Zhu, Y.W. and X.Z. wrote the manuscript with input from all authors.

Competing interests

The authors declare no competing interests.

Additional information

Supplementary information The online version contains supplementary material available at https://doi.org/10.1038/s41467-024-55359-8.

Correspondence and requests for materials should be addressed to Yong Wang, Liguo Zhang, Pu Gao or Qianhui Qu.

Peer review information *Nature Communications* thanks the anonymous reviewers for their contribution to the peer review of this work. A peer review file is available.